LA-UR-18-27420
Approved for public release; distribution is unlimited.

Title:	(U) Boundary Conditions for Ejecta Source Models with Stationary Velocity Distributions
Author(s):	Tregillis, Ian Lee
Intended for:	Report
Issued:	2018-08-03

LA-UR-YY-ZZZZZ

(U) Boundary Conditions for Ejecta Source Models with Stationary Velocity Distributions

I. L. Tregillis
Plasma Theory and Applications, XCP-6
Los Alamos National Laboratory
Los Alamos, NM 87545

Abstract

We show that certain apparently universal features of the piezoelectric voltage traces measured in HE-driven tin coupon experiments [1, 2] constrain the functional form of any ejecta source model with a stationary velocity distribution. Building on an analytic formalism that has been extensively documented elsewhere [3, 4, 5, 6, 7], we derive simple expressions for $V(t_a^0)$, $V'(t_a^0)$, and the discontinuity in $V(t_{break})$ where t_a^0 is the time of first ejecta arrival at the sensor and t_{break} is the "depletion" time for the fastest particles arriving at the sensor. These three quantities appear to be zero, or nearly so, in the Vogan voltage data [1] (modulo noise and any smoothing effects created by the circuit); however, the predicted voltages for this general class of source models do not automatically achieve these conditions unless special boundary conditions are met. Source models which violate these boundary conditions will produce voltage predictions at odds with the measurements. The RMI+SSVD ejecta source model in its current formulation satisfies none of these boundary conditions, and therefore predictions from a stationary-velocity-distribution approximation to the RMI+SSVD source model deviate significantly from the voltage data. This analysis suggests straightforward methods for potentially improving the predictions of the RMI+SSVD ejecta source model. We test this with a simple adjustment to the SSVD and find, as anticipated, the adjustment corrects three properties of the voltage prediction. Furthermore, the adjusted model's prediction for ejecta mass accumulation at the sensor exhibits a smoother and more gradual rise from the baseline than that produced by the original source model, thereby improving overall model/data agreement.

1 Basics

The results summarized in this section, as well as the formalism used throughout these notes, have been extensively documented elsewhere [3, 4, 5, 6, 7].

We consider the general class of ejecta source models featuring a stationary velocity distribution. Such models are described by source areal mass functions (AMFs) of the form

$$m_c(w, t_c) = m_0\, g(t_c)\, f(w) \tag{1.1}$$

or

$$m_c(w, t_c) = m_0\, g(t_c)\, f(w) \prod_{t_0}^{t_{cf}}(t_c) \tag{1.2}$$

where the boxcar function is used to terminate ejecta production at $t = t_{cf}$. Here $[m_0] = \text{mass} \cdot \text{area}^{-1}$, $[g] = \text{time}^{-1}$, and $[f] = \text{velocity}^{-1}$. For simplicity, and with no loss of generality, we set the shock breakout time at the free surface, $t_0 = 0$.

Technically, the RMI+SSVD ejecta source model contains a nonstationary velocity distribution, as the spike tip velocity approaches its asymptotic value (which is equated with the maximum ejecta relative velocity $\hat{w}$) over a finite period of time. However, investigation of the numerical solution from FLAG indicates that the spike tip velocity approaches the asymptotic value within approximately 100 ns; this is a much shorter interval than any interval required for the RMI model to produce the total integrated ejecta masses published for the Vogan [1] and Monfared shots [2] (i.e., $t_{cf} \gg 100$ ns). Thus, the spike tip velocity is effectively equal to its asymptotic value for most of the ejecta production interval; we use that observation to justify approximating the RMI+SSVD source model with a stationary velocity distribution. Previous investigations have shown [6] the analytic predictions from the RMI+SSVD source model approximated in this way exhibit strong agreement with numerical results obtained from FLAG calculations of the full (non-stationary) source model. The stationary approximation of the RMI+SSVD ejecta source model has

$$g(t_c) = \frac{2}{3}\,\frac{1}{t_c + \beta'\tau} \qquad f(w) = \frac{\xi \mathrm{e}^{-\frac{\xi w}{\hat{w}}} + 1}{(2 - \mathrm{e}^{-\xi})\hat{w}} \tag{1.3}$$

Given the above general form for m_c, the sensor AMF becomes

$$m_a(u, t) = m_0 \left(\frac{u}{u - u_{fs}}\right) g\left(\frac{ut - h}{u - u_{fs}}\right) f\left(u - u_{fs}\right) . \tag{1.4}$$

The general expression for the time-dependent pressure on the sensor, namely the arriving momentum flux, is

$$P(t) = \int_0^\infty m_a(u,t)\, u \, \mathrm{d}u = \int_{u(t_0,t)}^{\min\left(u(t_{cf},t),\hat{u}\right)} m_a(u,t)\, u \, \mathrm{d}u \tag{1.5}$$

where $u(t_c, t)$ denotes the lab-frame velocity of a particle created at time t_c and arriving (measured) at the sensor at time t. (Thus $u(t_0, t) = \frac{h}{t}$.) The upper limit of integration depends on the specifics of the problem. If the time domain of the measurement includes times such that $u(t_{cf}, t) > \hat{u}$ then the pressure calculation must be broken into multiple domains, as by definition no particles can have a lab-frame velocity exceeding $\hat{u}$. Indeed,

$$u(t_{cf},t) \geq \hat{u} \implies t \leq \frac{h + \hat{w}\, t_{cf}}{\hat{u}} = t(\hat{u}, t_{cf}) \equiv t_{break} \tag{1.6}$$

where $t(u, t_c)$ is the arrival time of particles created at time t_c with lab-frame velocity u; the most correct expression for the pressure on the sensor is therefore

$$P(t) = \begin{cases} \displaystyle\int_{\frac{h}{t}}^{\hat{u}} m_a(u,t)\, u \, \mathrm{d}u \equiv P_-(t) & t \leq t_{break} \\ \\ \displaystyle\int_{\frac{h}{t}}^{u(t_{cf},t)} m_a(u,t)\, u \, \mathrm{d}u \equiv P_+(t) & t \geq t_{break} \end{cases} . \tag{1.7}$$

Note $P_-(t_{break}) = P_+(t_{break})$ because $u(t_{cf}, t_{break}) = \hat{u}$.

The standard analysis which extracts an ejecta mass/area from the piezoelectric voltage utilizes the linear-regime relationship [8]

$$V(t) = A\, R\, S\, \frac{\mathrm{d}P}{\mathrm{d}t} \tag{1.8}$$

where A, R, and S are the collecting area of the piezoelectric pin, the terminating resistance of the circuit, and the piezoelectric sensitivity which is assumed to be well-approximated as a scalar for this application.

Finally, and for later reference, the complete Leibniz rule for differentiating an integral of this form is:

$$\frac{\mathrm{d}}{\mathrm{d}t} \int_{a(t)}^{b(t)} j(t,u)\, \mathrm{d}u = j\big[t, b(t)\big]\, \frac{\mathrm{d}b}{\mathrm{d}t} - j\big[t, a(t)\big]\, \frac{\mathrm{d}a}{\mathrm{d}t} + \int_{a(t)}^{b(t)} \frac{\partial\, j}{\partial\, t}(t,u)\, \mathrm{d}u\,. \tag{1.9}$$

In this application, $j(t, u) \equiv m_a(u, t)\, u$.

2 Two Properties of Piezoelectric Voltage Data

All published and available piezoelectric voltage traces relevant to these investigations [1] appear to exhibit two properties: they rise smoothly from the baseline, and they are everywhere continuous. (This inference could be incorrect, such as if noise and/or smoothing/filtering effects in the circuit are blurring underlying features.) While these properties are so basic, and so in keeping with our physical intuition, that they typically go unregarded, they are important and, as shown below, they are *not* automatically satisfied by the predictions of a given source model unless certain boundary conditions are met. It is a mistake to take these properties for granted: studying their implications yields important and powerful insights about an entire class of ejecta source models.

Quantitatively, these two properties encode three conditions:

- $V(t_a^0) = 0$
- $V'(t_a^0) = 0$
- $\lim_{t' \to t^+} V(t') = \lim_{t' \to t^-} V(t') \; \forall \; t$

where t_a^0 is the time of first ejecta arrival at the sensor.

The following sections investigate each of these requirements in turn.

3 Initial Voltage: $V(t_a^0)$

Because $t_a^0 < t_{break}$ we need only consider $P_-(t)$ in Eqn. 1.7. Application of the Leibniz rule yields

$$P'_-(t) = j(t, \hat{u}) \frac{\mathrm{d}\hat{u}}{\mathrm{d}t} - j\left(t, \frac{h}{t}\right) \frac{\mathrm{d}}{\mathrm{d}t}\frac{h}{t} + \int_{\frac{h}{t}}^{\hat{u}} \frac{\partial}{\partial t} j(t,u)\,\mathrm{d}u \tag{3.1}$$

$$= \frac{h^2}{t^3}\, m_a\left(\frac{h}{t}, t\right) + \int_{\frac{h}{t}}^{\hat{u}} u\left[\frac{\partial}{\partial t} m_a(u,t)\right] \mathrm{d}u\,. \tag{3.2}$$

Given $t_a^0 = \frac{h}{\hat{u}} \implies \frac{h}{t_a^0} = \hat{u}$, we obtain

$$\begin{aligned} P'_-(t_a^0) &= \frac{\hat{u}^3}{h}\, m_a(\hat{u}, t_a^0) = \frac{\hat{u}^3}{h}\, m_0 \left(\frac{\hat{u}}{\hat{u} - u_{fs}}\right) g\left(\frac{\hat{u}t_a^0 - h}{\hat{u} - u_{fs}}\right) f(\hat{u} - u_{fs}) \\ &= \frac{m_0}{h}\, \frac{\hat{u}^4}{\hat{w}}\, g(0)\, f(\hat{w}) \end{aligned}$$

and thus

$$V(t_a^0) = A\, R\, S\, \frac{m_0}{h}\, \frac{\hat{u}^4}{\hat{w}}\, g(0)\, f(\hat{w})\,. \tag{3.3}$$

It immediately follows that *any* stationary-velocity-distribution source model will produce $V(t_a^0) = 0$ *only* if $g(0) = 0$ or $f(\hat{w}) = 0$ or both.

We have obtained temporal and velocity boundary conditions required for *any* ejecta source model with a stationary velocity distribution to produce an initial voltage of 0 at the time of first ejecta arrival at the sensor. Any such model which fails to satisfy these conditions is *guaranteed* to predict a nonzero voltage at the time of first arrival, and thus predict a voltage trace which fails to rise smoothly from the baseline, contradicting the measurements.

The RMI+SSVD ejecta source model has

$$g(0) = \frac{2}{3\beta'\tau} \neq 0 \qquad f(\hat{w}) = \frac{\xi \mathrm{e}^{-\xi} + 1}{(2 - \mathrm{e}^{-\xi})\hat{w}} \neq 0\,.$$

Mathematica evaluations of the full analytic study of the RMI+SSVD source model agree with Eqn. 3.3. Note furthermore that Eqn. 3.3 is derived from first principles, for an entire class of source models: contrary to a common misconception, this result is *not* an artifact of constructing the analytic calculation to accommodate particular features of a specific dataset.

4 Initial Slope: $V'(t_a^0)$

A perfectly smooth rise from the baseline requires $V'(t_a^0) = 0$. We note for future reference that as a practical matter it is sufficient if $V'(t_a^0) \approx 0$ to within the measurement uncertainty. Applying the Leibniz rule to Eqn. 3.1 yields

$$P''_-(t) = -\frac{2h}{t^3}\, j\left(t, \frac{h}{t}\right) + \frac{h}{t^2}\, \frac{\mathrm{d}}{\mathrm{d}t} j\left(t, \frac{h}{t}\right)$$

$$+\left[\frac{\partial}{\partial t}j(t,u)\right]_{u=\hat{u}}\frac{\mathrm{d}\hat{u}}{\mathrm{d}t}-\left[\frac{\partial}{\partial t}j(t,u)\right]_{u=\frac{h}{t}}\frac{\mathrm{d}}{\mathrm{d}t}\frac{h}{t}+\int_{\frac{h}{t}}^{\hat{u}}\frac{\partial^2 j}{\partial t^2}(t,u)\,\mathrm{d}u\,.$$

The third term is identically zero at all times, and because $\frac{h}{t_a^0}=\hat{u}$ the fifth term is identically zero when $t=t_a^0$.

Given

$$j\left(t,\frac{h}{t}\right)=m_0\,g(0)\,f\left(\frac{h}{t}-u_{fs}\right)\frac{\left(\frac{h}{t}\right)^2}{\frac{h}{t}-u_{fs}}\,,$$

the first term evaluated at $t=t_a^0$ becomes

$$-2\,\frac{m_0}{h^2}\,\frac{\hat{u}^5}{\hat{w}}\,g(0)\,f(\hat{w})\,.$$

It follows that

$$\begin{aligned}\frac{\mathrm{d}}{\mathrm{d}t}j\left(t,\frac{h}{t}\right)=\frac{m_0}{h}&\left[\frac{\left(\frac{h}{t}\right)^4}{\left(\frac{h}{t}-u_{fs}\right)^2}-\frac{2\left(\frac{h}{t}\right)^3}{\frac{h}{t}-u_{fs}}\right]g(0)\,f\left(\frac{h}{t}-u_{fs}\right)\\&-\frac{m_0}{h}\,\frac{\left(\frac{h}{t}\right)^4}{\frac{h}{t}-u_{fs}}\,g(0)\,f'\left(\frac{h}{t}-u_{fs}\right)\end{aligned}$$

and thus the second term evaluated at $t=t_a^0$ becomes

$$\frac{m_0}{h^2}\left[\frac{\hat{u}^6}{\hat{w}^2}-2\frac{\hat{u}^5}{\hat{w}}\right]g(0)\,f(\hat{w})-\frac{m_0}{h^2}\,\frac{\hat{u}^6}{\hat{w}}\,g(0)\,f'(\hat{w})\,.$$

Furthermore,

$$\begin{aligned}\frac{\partial\, j}{\partial\, t}(t,u)&=m_0\,\frac{u^3}{(u-u_{fs})^2}\,g'\left(\frac{ut-h}{u-u_{fs}}\right)\,f(u-u_{fs})\\\implies\quad\left[\frac{\partial}{\partial t}j(t,u)\right]_{u=\frac{h}{t}}&=m_0\frac{\left(\frac{h}{t}\right)^3}{\left(\frac{h}{t}-u_{fs}\right)^2}\,g(0)\,f\left(\frac{h}{t}-u_{fs}\right)\end{aligned}$$

so the fourth term evaluated at $t=t_a^0$ is simply

$$\frac{m_0}{h}\,\frac{\hat{u}^5}{\hat{w}^2}\,g'(0)\,f(\hat{w})\,.$$

Combining these nonzero terms yields

$$V'(t_a^0) = A\,R\,S\left\{\frac{m_0}{h^2}\left[\frac{\hat{u}^6}{\hat{w}^2} - 4\frac{\hat{u}^5}{\hat{w}}\right] g(0)\, f(\hat{w}) + \frac{m_0}{h}\,\frac{\hat{u}^5}{\hat{w}^2}\, g'(0)\, f(\hat{w}) - \frac{m_0}{h^2}\,\frac{\hat{u}^6}{\hat{w}}\, g(0)\, f'(\hat{w})\right\}. \tag{4.1}$$

It immediately follows that *any* stationary-velocity-distribution source model will produce $V'(t_a^0) = 0$ *only* if

- $g(0) = g'(0) = 0$, or
- $g(0) = f(\hat{w}) = 0$, or
- $f(\hat{w}) = f'(\hat{w}) = 0$

or some combination thereof.

We have obtained temporal and velocity boundary conditions required for *any* ejecta source model with a stationary velocity distribution to produce a voltage trace with initial slope 0 at the time of first ejecta arrival at the sensor. Any such model which fails to satisfy these conditions is *guaranteed* to predict a nonzero slope at the time of first arrival.

In addition to $g(0) \neq 0$ and $f(\hat{w}) \neq 0$ as shown above, the RMI+SSVD ejecta source model has

$$g'(0) = -\frac{2}{3(\beta'\tau)^2} \neq 0 \qquad f'(\hat{w}) = -\frac{\xi^2}{\hat{w}^2}\,\frac{\mathrm{e}^{-\xi}}{2 - \mathrm{e}^{-\xi}} \approx 0$$

Mathematica evaluations of the full analytic study of the RMI+SSVD source model agree with Eqn. 4.1. Note furthermore that Eqn. 4.1 is derived from first principles, for an entire class of source models: this result is *not* an artifact of constructing the analytic calculation to accommodate particular features of a specific dataset.

5 Continuity: $\lim_{t' \to t^+} V(t') = \lim_{t' \to t^-} V(t')\ \forall\ t$

Clearly $P_-(t)$, $P_+(t)$, and their derivatives are continuous functions. The only measurement time at which the pressure derivative might become discontinuous is

$t = t_{break}$. In other words $P_-(t_{break}) = P_+(t_{break})$ does not guarantee $P'_-(t_{break}) = P'_+(t_{break})$.

Applying the Leibniz rule to both branches of $P(t)$ yields

$$P'_-(t) = j(t, \hat{u}) \frac{\mathrm{d}\hat{u}}{\mathrm{d}t} - j\left(t, \frac{h}{t}\right) \frac{\mathrm{d}}{\mathrm{d}t}\frac{h}{t} + \int_{\frac{h}{t}}^{\hat{u}} \frac{\partial}{\partial t} j(t, u)\, \mathrm{d}u$$

$$P'_+(t) = j\left[t, u(t_{cf}, t)\right] \frac{\mathrm{d}}{\mathrm{d}t} u(t_{cf}, t) - j\left(t, \frac{h}{t}\right) \frac{\mathrm{d}}{\mathrm{d}t}\frac{h}{t} + \int_{\frac{h}{t}}^{u(t_{cf},t)} \frac{\partial}{\partial t} j(t, u)\, \mathrm{d}u$$

and thus at the time of interest

$$\begin{aligned} P'_+(t_{break}) - P'_-(t_{break}) &= j\left[t_{break}, u(t_{cf}, t_{break})\right] \left[\frac{\mathrm{d}}{\mathrm{d}t} u(t_{cf}, t)\right]_{t=t_{break}} \\ &= j(t_{break}, \hat{u}) \left[\frac{\mathrm{d}}{\mathrm{d}t} u(t_{cf}, t)\right]_{t=t_{break}} . \end{aligned}$$

We find

$$\frac{\hat{u} t_{break} - h}{\hat{u} - u_{fs}} = t_{cf}$$

and thus

$$j(t_{break}, \hat{u}) = m_0 \frac{\hat{u}^2}{\hat{w}}\, g(t_{cf})\, f(\hat{w})\,,$$

while

$$u(t_{cf}, t) \equiv \frac{h - u_{fs} t_{cf}}{t - t_{cf}} \implies \left[\frac{\mathrm{d}}{\mathrm{d}t} u(t_{cf}, t)\right]_{t=t_{break}} = -\frac{\hat{u}^2}{h - u_{fs} t_{cf}}\,.$$

(Note $h - u_{fs} t_{cf} = 0$ requires an implausible, and possibly unphysical, duration for the ejecta production interval at odds with observations.)

The velocity discontinuity at $t = t_{break}$ is therefore

$$\Delta V(t_{break}) = A\, R\, S \frac{m_0}{h - u_{fs} t_{cf}} \frac{\hat{u}^4}{\hat{w}}\, g(t_{cf})\, f(\hat{w}) \tag{5.1}$$

from which it immediately follows that the predicted voltage trace will be continuous at $t = t_{break}$ only if $g(t_{cf}) = 0$ or $f(\hat{w}) = 0$ or both.

We have obtained temporal and velocity boundary conditions required for any ejecta source model with a stationary velocity distribution to produce a fully continuous

voltage trace. Any such model which fails to satisfy these conditions is *guaranteed* to predict a voltage that is discontinuous at $t = t_{break}$, contradicting the measurements.

Note that the condition $g(t_{cf}) = 0$ indicates a model which naturally terminates ejecta production without resorting to an externally imposed condition such as the boxcar function in Eqn. 1.2. Therefore any model which does *not* embody a natural termination to the production process will exhibit a discontinuous voltage unless $f(\hat{w}) = 0$.

The RMI+SSVD ejecta source model has

$$g(t_{cf}) = \frac{2}{3}\,\frac{1}{t_{cf} + \beta'\tau} \neq 0 \qquad\qquad f(\hat{w}) = \frac{\xi \mathrm{e}^{-\xi} + 1}{(2 - \mathrm{e}^{-\xi})\hat{w}} \neq 0\,.$$

Mathematica evaluations of the full analytic study of the RMI+SSVD source model agree with Eqn. 5.1. Note furthermore that Eqn. 5.1 is derived from first principles, for an entire class of source models. Once again, this result is *not* an artifact of constructing the analytic calculation to accommodate particular features of a specific dataset.

5.1 Insights from the Integration Domain

The discontinuity in $P'(t_{break})$ may seem counterintuitive. The derivation above presents a mathematical argument for the existence of the discontinuity. A more physically motivated insight can be obtained by considering the domain of integration used to compute $P(t)$.

A quantitative example is shown in Fig. 1, where the domain of integration has been constructed for Vogan shot 12 [1]. We see that t_{break} is

- the time before which $u(t_{cf}, t) > \hat{u}$, *and*
- the time at which the highest-velocity particles stop arriving at the sensor, i.e., the "depletion time" for particles with $u = \hat{u}$.

In a sense, t_{break} represents the time at which the *sensor* first sees an indication that ejecta production at the *source* did not persist indefinitely.

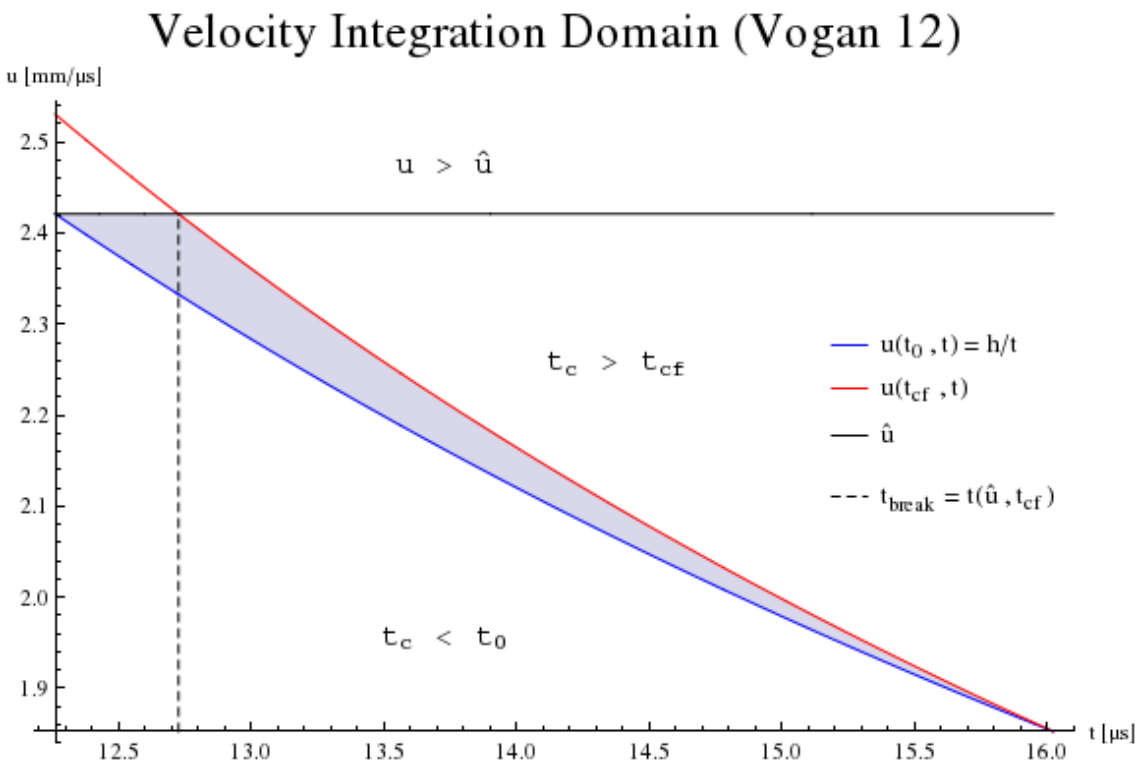

Figure 1: Velocity integration domain for Eqn. 1.5, computed for Vogan et al. shot 12 [1]. The axes are measurement (arrival) time, t, and lab-frame velocity, u. The shaded region is the domain of integration. The red line represents the velocity of particles created at time t_{cf}; the blue line is the velocity of particles created at time t_0. The dashed line, t_{break}, represents the arrival time of particles created at time t_{cf} with lab-frame velocity $\hat{u}$. In the case of a stationary velocity distribution, this is the last possible arrival time for particles with $u = \hat{u}$.

6 Voltage Prediction Example

Fig. 2 shows the analytically computed voltage prediction from the RMI+SSVD ejecta source model overlaid with the actual voltage measurement for Vogan shot 12 [1]. The details of the analytic voltage calculation have been documented elsewhere [5]. The model prediction is clearly discrepant from the observation in all three quantities considered here: $V(t_a^0) \neq 0$, $V'(t_a^0) \neq 0$, and $\Delta V(t_{break}) \neq 0$ because the present formulation of the RMI+SSVD source model adheres to none of the boundary conditions derived above.

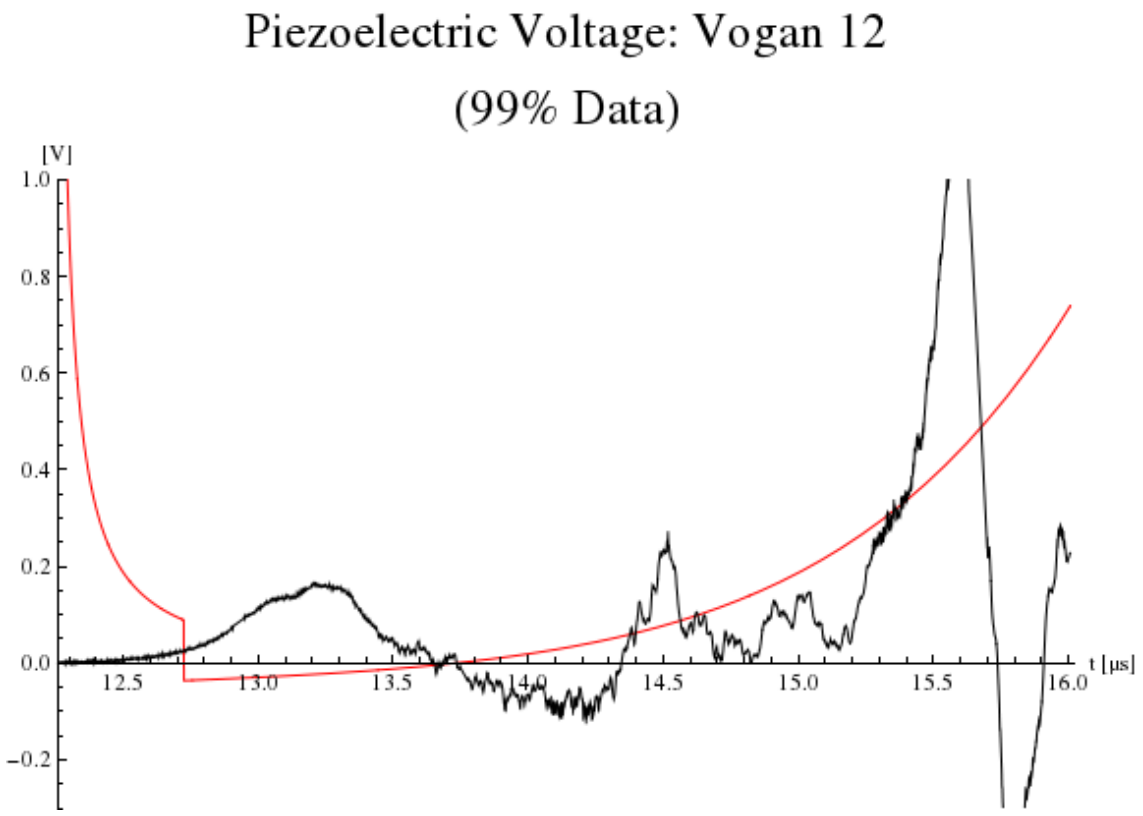

Figure 2: Measured (black) and analytically computed (red) piezoelectric voltages for Vogan shot 12 [1]. The analytic calculation used the RMI+SSVD ejecta source model. The model prediction is discrepant from the observation in $V(t_a^0)$, $V'(t_a^0)$, and $\Delta V(t_{break})$ because the source model does not embody the requisite boundary conditions.

7 Boundary Conditions from Voltage

We have derived a set of simple and physically plausible boundary conditions on a general class of ejecta source models. These conditons are required if such source models are to produce piezoelectric voltage traces consistent with several apparently universal properties of the data.

Given the general form for ejecta source models with a stationary velocity distribu-

tion

$$m_c(w, t_c) = m_0\, g(t_c)\, f(w)$$

we have shown

- $V(t_a^0) = 0$ requires $g(0) = 0$, $f(\hat{w}) = 0$, or both;
- $V'(t_a^0) = 0$ requires $g(0) = g'(0) = 0$, or $g(0) = f(\hat{w}) = 0$, or $f(\hat{w}) = f'(\hat{w}) = 0$;
- $\Delta V(t_{break}) = 0$ requires $g(t_{cf}) = 0$, $f(\hat{w}) = 0$, or both

where $\hat{w}$ is the maximum ejecta velocity relative to the free surface, t_a^0 is the time of first ejecta arrival at the sensor, t_{break} is the "depletion time" of the highest velocity particles arriving at the sensor, and t_{cf} is the time at which ejecta production terminates.

Boundary condition combinations that simultaneously satisfy all three voltage properties include:

- $g(0) = f(\hat{w}) = 0$
- $f(\hat{w}) = f'(\hat{w}) = 0$: As shown below, this might be approximately achieved by applying a constant shift to the SSVD.
- $g(0) = g'(0) = g(t_{cf}) = 0$: This suggests a model incorporating a smooth "start-up" and a natural termination at t_{cf}.

The physicality of $g(0) = 0$ and $g'(0) = 0$ is debatable, particularly for an impulsive, shock-driven process. This is illustrated by considering the limiting case of truly instantaneous production, where $g(t_c)$ becomes $\delta(t_c)$. A natural termination, i.e., $g(t_{cf}^*) = 0$ for some termination time t_{cf}^* *determinated by the model*, would resolve difficulties documented elsewhere [7], and indeed a physics-based determination of t_{cf}^* is a crucial question for any source model. But, given the questionable physicality of the "smooth start-up" scenario, we lay it aside for now.

This leaves $f(\hat{w}) = 0$ and $f'(\hat{w}) = 0$ as the boundary conditions required for imbuing the predicted voltage trace with the requisite properties. As shown in Section 9, both conditions can be achieved (or very nearly so) with a single simple modification to the SSVD.

8 Boundary Conditions From Mass

When $t \leq t_{break}$, the true ejecta mass accumulation at the sensor is

$$m_t(t) = \int_{t_a^0}^{t} \mathrm{d}t' \int_{\frac{h}{t'}}^{\hat{u}} m_a(u, t') \, \mathrm{d}u$$

so

$$m_t'(t) = \int_{\frac{h}{t}}^{\hat{u}} m_a(u, t) \, \mathrm{d}u \, .$$

Because $t_0^a \equiv \frac{h}{\hat{u}}$, this immediately yields

$$m_t'(t_a^0) = 0 \, , \tag{8.1}$$

indicating that the initial slope of the true mass accumulation is always guaranteed to be zero. Application of the Leibniz rule to the above expression for $m_t'(t)$ yields

$$m_t''(t) = m_a(\hat{u}, t) \frac{\mathrm{d}\hat{u}}{\mathrm{d}t} - m_a \left[\frac{h}{t}, t \right] \frac{\mathrm{d}}{\mathrm{d}t} \left(\frac{h}{t} \right) + \int_{\frac{h}{t}}^{\hat{u}} \left[\frac{\partial}{\partial t} m_a(u, t) \right] \, \mathrm{d}u$$

so

$$m_t''(t_a^0) = \frac{h}{(t_a^0)^2} \, m_a \left(\frac{h}{t_a^0}, t_a^0 \right) = \frac{m_0}{h} \, \frac{\hat{u}^3}{\hat{w}} \, g(0) \, f(\hat{w}) \, . \tag{8.2}$$

A similar analysis for the inferred mass accumulation finds

$$m_i'(t_a^0) = m_t'(t_a^0) = 0 \qquad m_i''(t_a^0) = 2 \, m_t''(t_a^0) = 2 \, \frac{m_0}{h} \, \frac{\hat{u}^3}{\hat{w}} \, g(0) \, f(\hat{w}) \, . \tag{8.3}$$

This analysis indicates that the true and inferred mass accumulations will have $m_{t,i}(t_a^0) = m_{t,i}'(t_a^0) = m_{t,i}''(t_a^0) = 0$ and thus a very smooth rise from the baseline if $g(0) = 0$ or $f(\hat{w}) = 0$. Stationary-velocity-distribution source models that do not meet these conditions are guaranteed to have $m_{t,i}''(t_a^0) \neq 0$.

Interestingly, the RMI+SSVD model, which does not satisfy these boundary conditions, has long been known to predict a mass accumulation that rises more rapidly from the baseline than is typically seen in the data for low-kh_0 shots [5].

9 Test: A Tweak to SSVD

The stationary approximation to SSVD yields the velocity distribution $f(w)$ listed in Eqn. 1.3. When incorporated in a source model, this continuous function must obviously be truncated at $w = \hat{w}$, lest the model produce ejecta particles with velocities exceeding the highest velocities observed in a given experiment. This is why $f(\hat{w}) \neq 0$ as described above; an example is plotted in Fig. 3. We note that $f'(\hat{w}) \approx 0$. This suggests the desired boundary conditions $f(\hat{w}) = f'(\hat{w}) = 0$ could be approximately achieved simply by subtracting a constant from $f(w)$ and renormalizing the result. The result of this operation is also plotted in Fig. 3.

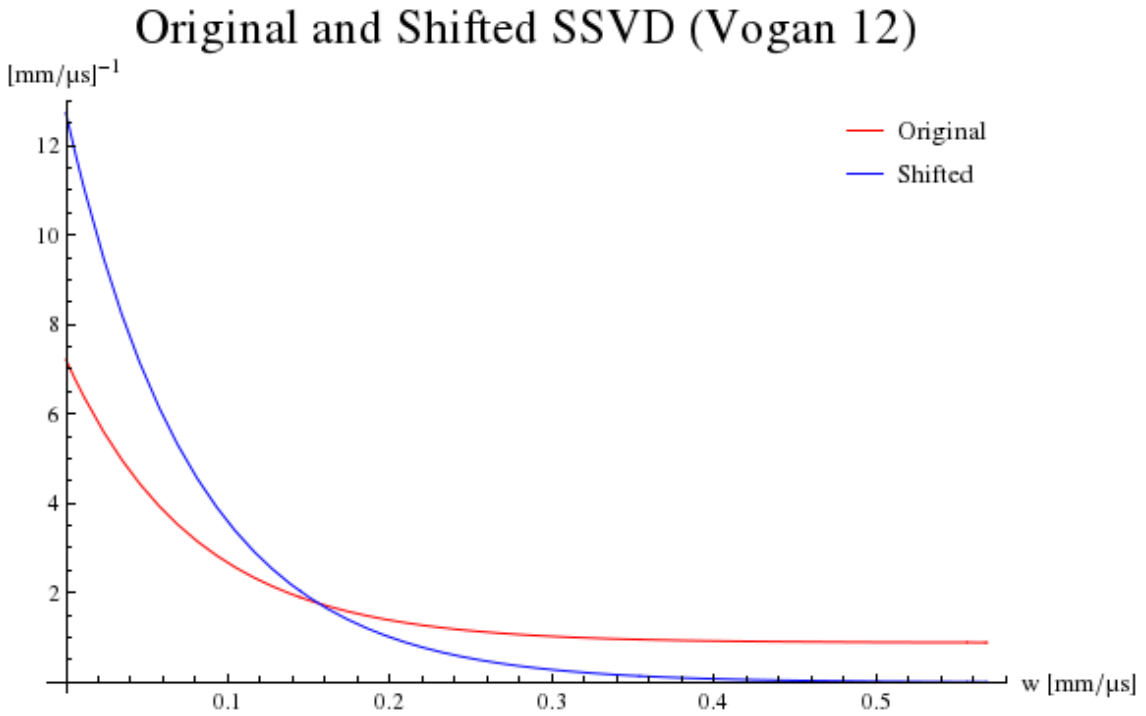

Figure 3: Red: SSVD defined by Eqn. 1.3 ($f(w)$) for Vogan shot 12 [1]. Blue: shifted and renormalized SSVD ($\tilde{f}(w)$) for the same shot.

We define a new velocity distribution

$$\tilde{f}(w) = \kappa \, [f(w) - f(\hat{w})] \qquad \kappa = \frac{2 - \mathrm{e}^{-\xi}}{1 - (\xi + 1)\mathrm{e}^{-\xi}} \tag{9.1}$$

where the normalization factor κ is required to ensure

$$\int_0^{\hat{w}} \tilde{f}(w)\,\mathrm{d}w = 1\,.$$

Now

$$\tilde{f}(\hat{w}) = 0 \qquad \tilde{f}'(\hat{w}) \approx 0\,.$$

The new (adjusted) source and sensor AMFs become

$$\begin{aligned}\tilde{m_c}(w,t_c) &= m_0\,g(t_c)\,\tilde{f}(w) = \kappa\,m_0\,g(t_c)\,f(w) - [\kappa f(\hat{w})]\;m_0\,g(t_c)\\ &= \kappa\,m_c(w,t_c) - \nu\left\{\text{non}-\text{exponential terms in}\,m_c(w,t_c)\right\} \qquad (9.2)\\ \tilde{m_a}(u,t) &= \kappa\,m_a(u,t) - \nu\left\{\text{non}-\text{exponential terms in}\,m_a(u,t)\right\} \qquad (9.3)\end{aligned}$$

where

$$\nu = (1+\xi \mathrm{e}^{-\xi})\,\kappa = \frac{(1+\xi\mathrm{e}^{-\xi})(2-\mathrm{e}^{-\xi})}{1-(\xi+1)\mathrm{e}^{-\xi}}\,. \qquad (9.4)$$

(The exponential and non-exponential terms in m_c are self-evident from multiplying $g(t_c)$ and $f(w)$ in Eqn. 1.3. The associated terms in m_a follow accordingly.) This schematic description of the adjusted AMFs makes it straightforward to compute the adjusted true and inferred cumulative ejecta masses at the sensor ($\tilde{m_t}(t)$ and $\tilde{m_i}(t)$, respectively); the adjusted pressure on the piezoelectric sensor ($\tilde{P}(t)$); and the adjusted voltage prediction ($\tilde{V}(t)$) from their counterparts calculated with the original (unadjusted) SSVD.

$V(t)$ and $\tilde{V}(t)$ are co-plotted alongside the data for Vogan shot 12 [1] in Fig. 4. We see that adjusting the SSVD to embody the desired boundary conditions has corrected three features of the voltage prediction *exactly* as predicted:

- $V(t_a^0) = 0$
- $V'(t_a^0) \approx 0$ (equivalence is approximate because $\tilde{f}'(\hat{w}) \approx 0$)
- $\Delta V(t_{break}) = 0$

The original voltage prediction for shot 12 has $V'(t_a^0) = -165$ V/μs; the adjusted voltage prediction has $\tilde{V}'(t_a^0) = 0.08$ V/μs.

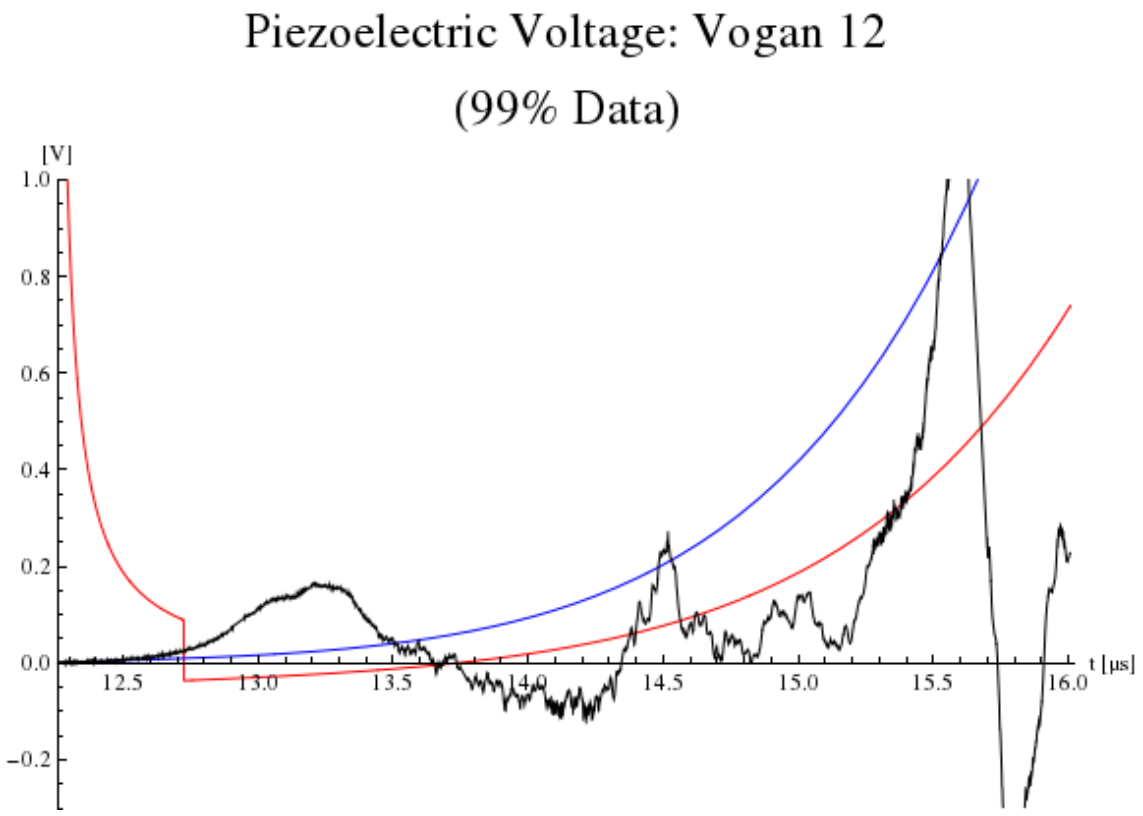

Figure 4: Black: piezoelectric voltage measurement for Vogan shot 12 [1]. Red: analytically computed voltage prediction from the RMI+SSVD ejecta source model. Again, the model prediction is discrepant from the observation in $V(t_a^0)$, $V'(t_a^0)$, and $\Delta V(t_{break})$ because the source model does not embody the requisite boundary conditions. Blue: voltage prediction computing using the shifted SSVD, $\tilde{f}(w)$. The adjusted voltage prediction exhibits $V(t_a^0) = 0$, $V'(t_a^0) \approx 0$, and $\Delta V(t_{break}) = 0$.

The original and adjusted model predictions for the cumulative ejecta mass are co-plotted alongside the thresholded (99%) mass data [7, 9] for Vogan shot 12 [1] in Fig. 5. As expected, adjusting the SSVD to ensure $m''(t_a^0) = 0$ softened the initial mass accumulation at the sensor. (See also Figs. 8 and 9.) As shown in Section 10, this softening is generally beneficial to the model.

(To simplify comparison, all analytic mass calculations were constructed to match the thresholded data at the endpoints, t_{99} and $t_a^1 = t_{fs} = \frac{h}{u_{fs}}$, where t_{99} marks the empirical transition from the earliest arriving 1% of the ejecta mass to the subsequent 99%. This is done because the source model targets 99% of the mass [9]. Note that

for low-kh$_0$ shots, the RMI model's asymptotic spike-tip velocity correctly predicts the true first arrival time ($t_a^0 = \frac{h}{\tilde{u}} = \frac{h}{u_{fs}+\sqrt{3}\dot{\eta}_0^s}$), but not t_{99}.)

The results of this test are dramatic: **one** modification to the SSVD improved **four** predictions of the RMI+SSVD source model.

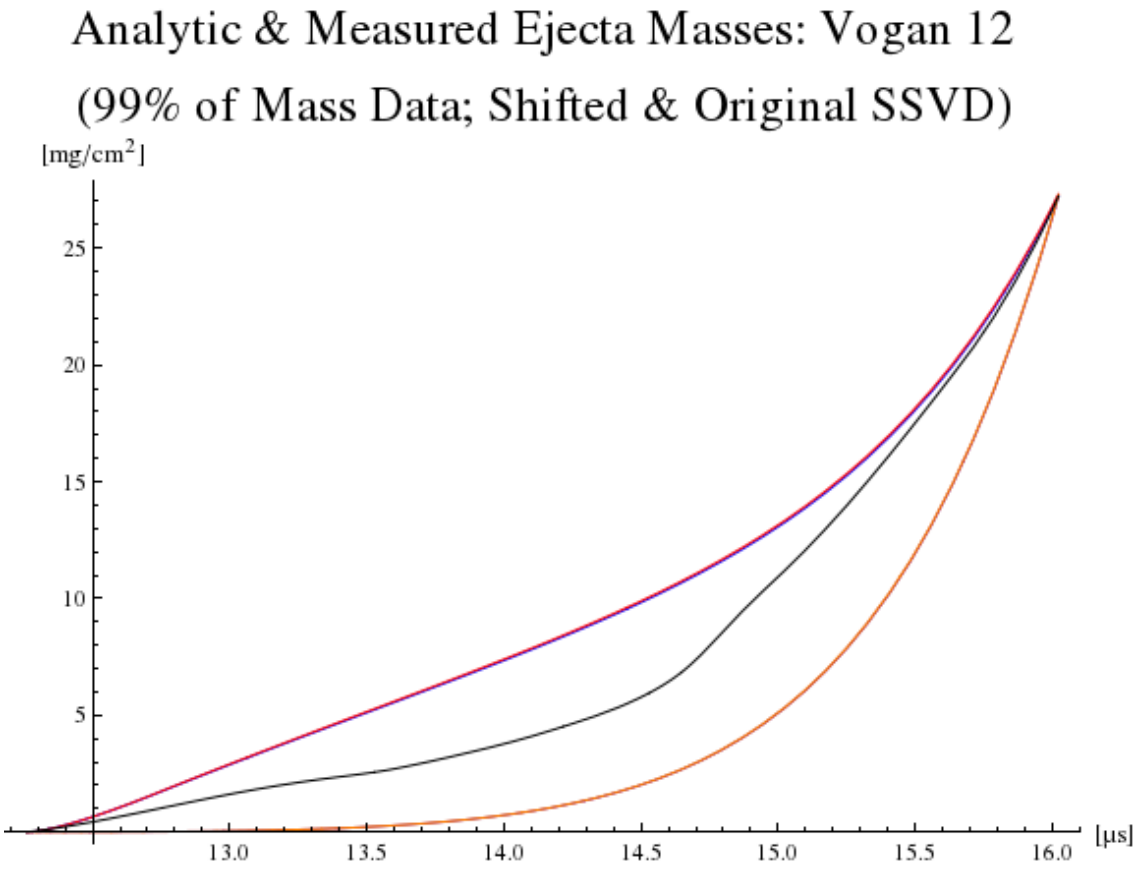

Figure 5: Black: piezoelectric mass measurement for Vogan shot 12 [1], thresholded at 99% of the mass (i.e., the earliest-arriving 1% of the mass has been removed from consideration). Blue: true mass accumulation ($m_t(t)$) at the sensor for an ejecta source model using the original SSVD, $f(w)$. Red: piezoelectrically inferred mass accumulation ($m_i(t)$) at the sensor for an ejecta source model using the original SSVD, $f(w)$. Purple: true mass accumulation ($\tilde{m}_t(t)$) at the sensor for an ejecta source model using the adjusted SSVD, $\tilde{f}(w)$. Orange: piezoelectrically inferred mass accumulation ($\tilde{m}_i(t)$) at the sensor for an ejecta source model using the adjusted SSVD, $\tilde{f}(w)$. The blue/red and purple/orange pairs are nearly indistinguishable because the epistemic uncertainty incurred by the assumption of instantaneous ejecta production (which is folded into the piezoelectric analysis that converts voltage to mass) is negligible. All analytic calculations used a tuned t_{cf} value and were constructed so that the first ejecta arrival at the sensor coincided with t_{99}.

10 Model Compatibility Scores

To quantify the impact of this adjustment to the SSVD, we compute a set of hypothetical "compatibility scores" to quantify the level of agreement between the model prediction and data in a variety of scenarios. For a given shot and a given specification of the time-dependent piezoelectric measurement uncertainty in the experiment, we compute the percentage of ejecta mass for which a model's prediction is consistent with (i.e., falls within) those uncertainty bounds. This produces a number between 0 and 100: 0 indicates a worst-case scenario where the model is *never* consistent with the data, while 100 indicates the ideal case where the model is consistent *everywhere*. (Appendix A contains an example compatibility score calculation.)

We consider two hypothetical uncertainty models for computing these compatibility scores. Both are motivated by the observation that the published 1σ measurement uncertainties on the final, time-integrated ejecta mass measurements via lithium-niobate (LN) piezoelectric sensors is approximately $\pm 10\%$ [2, 10, 11]. The first scenario assumes the LN measurement uncertainty is a constant $\pm 10\%$. The second scenario assumes it begins with the largest meaningful value ($\pm 100\%$) at the first measurement time then declines linearly to the known 1σ uncertainty at the final measurement time. These hypothetical uncertainy variations are used for purposes of exploration, and are not necessarily representative of the true time dependence.

We also apply several methods for setting the ejecta production interval, t_{cf}, in the source model. This value may be tuned separately for each individual shot, such that the model prediction for the total mass produced matches 99% of the published measured value for that shot. Alternatively, the values may be prescribed without regard to the details of the shot. PEM has recommended using $t_{cf} = a \cdot \frac{\lambda}{u_{fs}}$ where $a = 40$ [12]. Here we have used $a = 30$, 40, & 50 for the prescribed t_{cf} values. This $\pm 25\%$ variation in a changes the mass predicted by the RMI model by $\approx \pm^{8}_{10}\%$, meaning these t_{cf} values are indistiguishable within 1σ error bars on the mass data. Table 1 lists the various t_{cf} values for the shots under consideration.

Table 2 summarizes the compatibility scores obtained from the original RMI+SSVD ejecta source model for these eight hypothetical scenarios (two uncertainty models $\times$ four methods for setting t_{cf}). Table 3 represents compatibility values for the same scenarios, now calculated using the adjusted SSVD.

							prescribed $t_{cf} = a\lambda/u^{\ddagger}_{fs}$		
Shot #	kh_0	$0.99{\cdot}\rho_A(t_{fs})^{\dagger}$ [mg cm$^-$2]	$m_0^{\ddagger}$ [mg cm$^-$2]	$\beta'^{\ddagger}$	$\tau^{\ddagger}$ [ns]	tuned t_{cf} [μs]	$a = 30$ [μs]	$a = 40$ [μs]	$a = 50$ [μs]
6	0.19	2.48	1.28	1.56	6.45	0.17	0.26	0.35	0.44
10	0.08	15.54	8.99	1.57	104.2	2.02	1.88	2.50	3.13
11	0.22	20.79	8.38	1.56	37.8	2.38	1.78	2.37	2.96
12	0.25	27.23	12.4	1.56	49.0	1.98	2.62	3.49	4.36

Table 1: Relevant parameters for four Vogan et al. shots [1]. †Final thresholded (i.e., 99%) mass values derived from the Vogan/Buttler dataset; compare [1, Fig. 11]. ‡Values derived from the perturbation λ and kh_0 values; u_{fs} values required to match the published $\rho_A(t_{fs})$ in the dataset; and the shock velocity in associated FLAG calculations.

		Constant 10%†				100% $\rightarrow$ 10%‡			
Shot	kh_0	Tuned	$a = 30$	$a = 40$	$a = 50$	Tuned	$a = 30$	$a = 40$	$a = 50$
6	0.19	43.8	$\approx$0	$\approx$0	$\approx$0	63.8	26.1	$\approx$0	$\approx$0
10	0.08	32.6	38.2	9.1	$\approx$0	52.2	56.7	28.2	$\approx$0
11	0.22	15.1	26.4	15.2	6.6	17.8	36.6	23.9	8.3
12	0.25	49.6	16.8	$\approx$0	$\approx$0	76.3	65.5	30.4	5.5

Table 2: Percentage of time-dependent ejecta mass the RMI+SSVD source model places within given uncertainty bounds on the thresholded piezoelectric data. Values of 0% are approximate, owing to artificially enforced agreement between the theoretical and measured first-arrival times. †Hypothetical uncertainty is $\pm$10% at all measurement times. ‡Hypothetical uncertainty is $\pm$100% at the time of first ejecta arrival, declining linearly to $\pm$10% at the final measurement time.

		Constant 10%				100% $\rightarrow$ 10%			
Shot	kh_0	Tuned	$a = 30$	$a = 40$	$a = 50$	Tuned	$a = 30$	$a = 40$	$a = 50$
6	0.19	13.2	20.3	21.8	39.1	20.8	47.2	20.2	52.5
10	0.08	22.6	36.2	18.3	29.9	32.2	50.3	27.5	50.4
11	0.22	83.7	89.0	68.9	88.8	83.6	89.0	47.0	89.2
12	0.25	15.2	22.4	22.3	30.4	17.8	29.8	15.0	29.7

Table 3: As Table 2, now computed using the adjusted SSVD (Eqn. 9.1).

Table 4 summarizes the change in model compatibility scores when moving from the original SSVD to the adjusted SSVD. Positive numbers represent increased scores and therefore an increased level of model/data agreement in these scenarios. A gallery of plots showing the relevant model predictions is presented in Appendix B.

		Constant 10%				100% → 10%			
Shot	kh_0	Tuned	$a = 30$	$a = 40$	$a = 50$	Tuned	$a = 30$	$a = 40$	$a = 50$
6	0.19	-30.6	20.3	21.8	39.1	-43.0	21.1	20.2	52.5
10	0.08	-10.0	-2.0	9.2	29.9	-20.0	-6.4	-0.7	50.4
11	0.22	68.6	62.6	53.7	82.2	65.8	52.4	23.1	80.9
12	0.25	-34.4	5.6	22.3	30.4	-58.5	-35.7	-15.4	24.2

Table 4: Change in model compatibility scores, computed from Tables 2 and 3.

A Example: Compatibility Score Calculation

In this section, we illustrate how the relevant model compatibility scores for Vogan et al. shot 12 [1] (see Fig. 5) were computed in Tables 2 and 3.

First, we compute the minimum measurement uncertainty required for the model predictions to agree with the data at each time. Here, "agreement" means the model prediction lies within the range of values defined by data + uncertainty. Expressed as a percentage, this is

$$\Delta(t) = 100.0 \times \left[\frac{\text{model}(t)}{\text{data}(t)} - 1.0\right] . \tag{A.1}$$

We convert this to a function of the delivered mass fraction, as shown in Fig. 6.

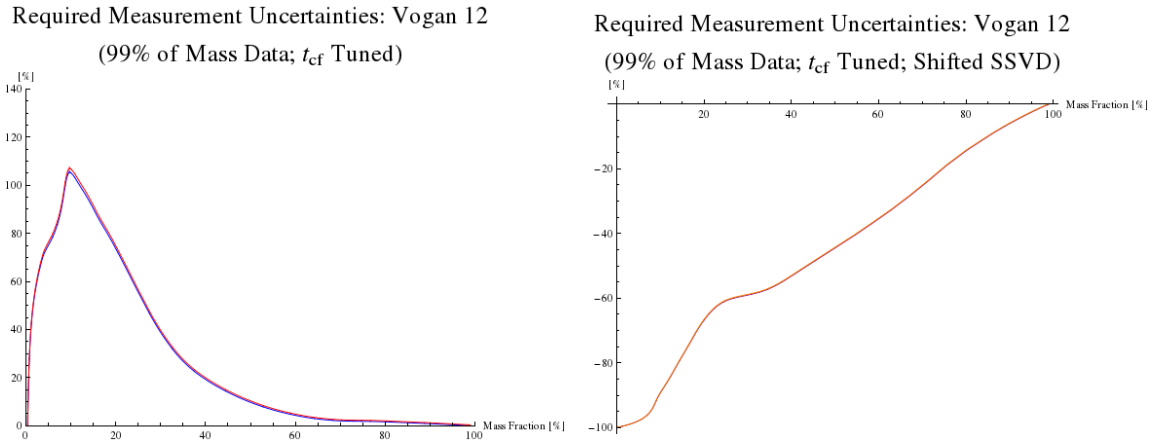

Figure 6: Minimum measurement uncertainties required for model/data agreement. Results for both true (m_t, $\tilde{m}_t$) and inferred (m_i, $\tilde{m}_i$) masses are shown, but only the inferred values are used to compute the compatibility score. Left: Original SSVD. Right: Adjusted SSVD. Compare Fig. 5.

Next, for a given hypothetical uncertainty model, we construct a function that is 1 when the model prediction lies within that uncertainty of the data, and 0 otherwise. A result for the constant ±10% scenario applied to the model prediction computed using the adjusted SSVD is shown in Fig. 7.

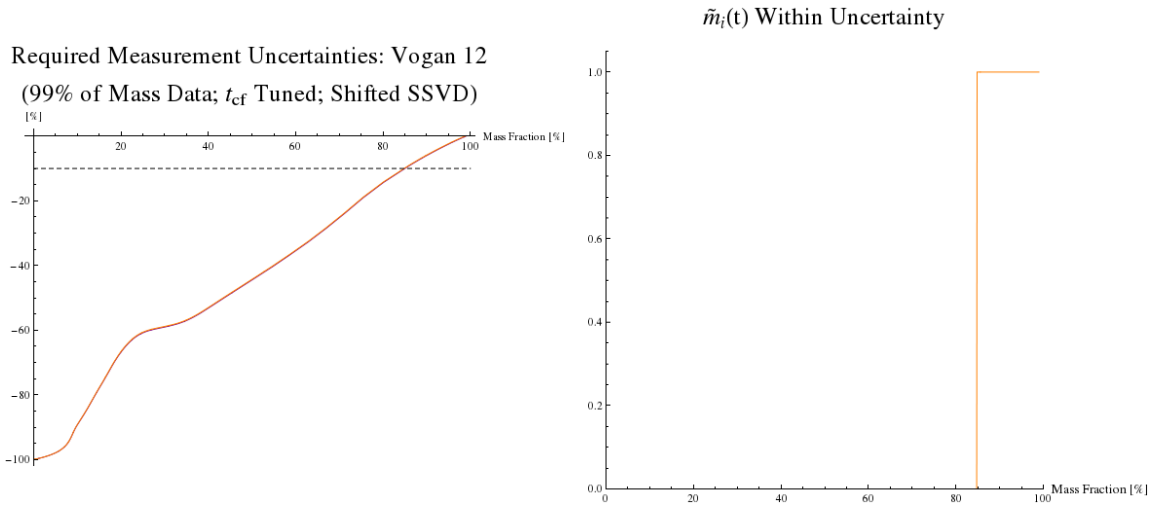

Figure 7: Left: minimum measurement uncertainties required for compatibility between $\tilde{m}_i(t)$ and the thresholded data, overlaid with bounds at ±10%. Right: Mass fraction domain where the required minimum uncertainties fall within the bounds of the ±10% scenario.

The integral of this function is the compatibility score. For Vogan et al. shot 12 [1], a tuned t_{cf} value, the adjusted SSVD, and the constant ±10% measurement uncertainty scenario, this yields 15.2, as listed in Table 3.

B Gallery of m_t, m_i, $\tilde{m}_t$, & $\tilde{m}_i$ Plots (Tuned t_{cf})

Table 4 lists how the model compatibility scores change when the velocity distribution underlying the analytic calculations moves from the original SSVD specification (Eqn. 1.3) to the shifted SSVD (Eqn. 9.1). These changes are more easily understood by comparing the analytically computed $m_i(t)$ and $\tilde{m}_i(t)$ for each shot. These results (as well as $m_t(t)$ and $\tilde{m}_t(t)$) are plotted in Figs. 8 and 9, for four low-kh_0 shots in the Vogan et al. [1] dataset, using a tuned t_{cf} value for each.

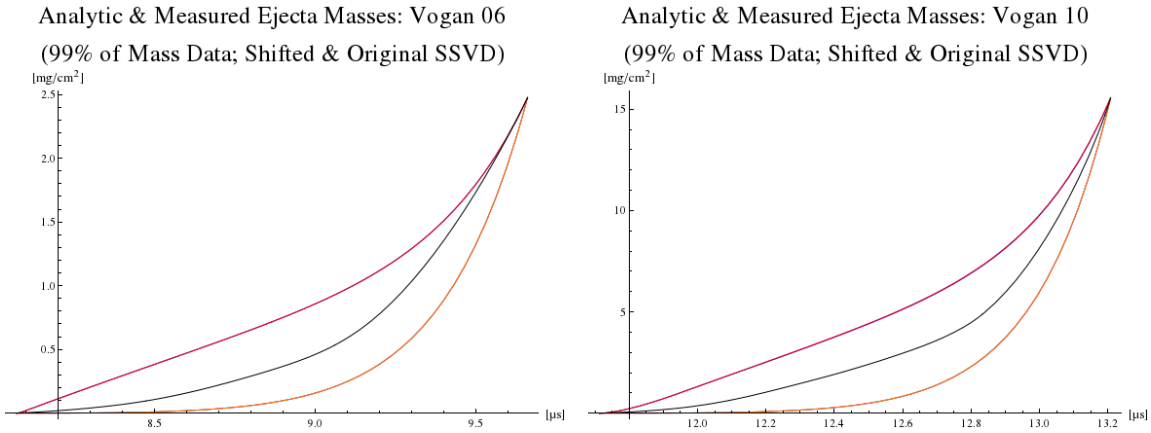

Figure 8: Left: Shot 6 ($kh_0 \approx 0.19$). Right: Shot 10 ($kh_0 \approx 0.08$). See Fig. 5 for full caption.

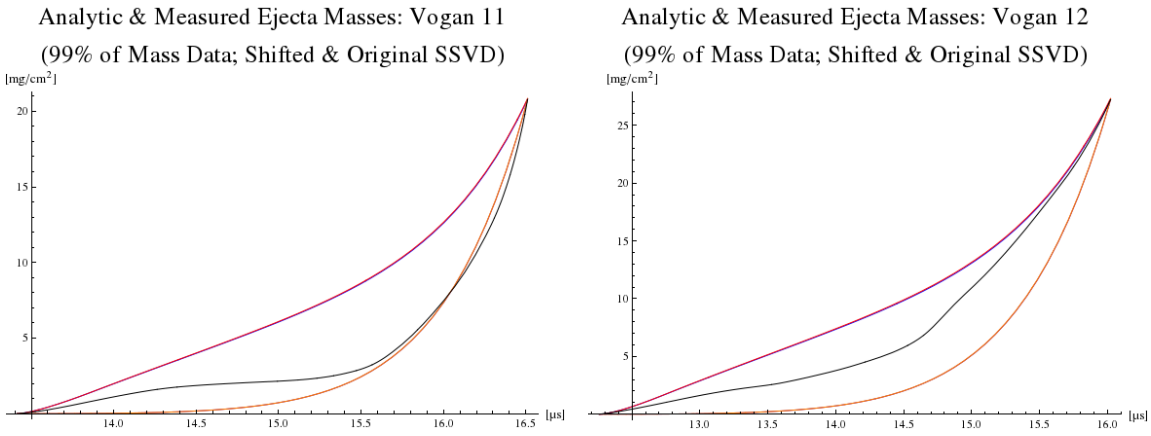

Figure 9: Left: Shot 11 ($kh_0 \approx 0.22$). Right: Shot 12 ($kh_0 \approx 0.25$). See Fig. 5 for full caption.

We reiterate that these analytic calculations were constructed to match the thresholded data at both endpoints, t_{99} and t_{fs}. In this framework, the RMI+SSVD source model's prediction for the true and inferred cumulative ejecta masses at the sensor lie everywhere above the data, while the model predictions computed using the adjusted velocity distribution lie almost everywhere below the data. In some cases, the adjustment is extremely beneficial, as with Shot 11 ($kh_0 \approx 0.22$), where the model compatibility score increases by 66-69%; in other cases, the adjustment is detrimental, as with Shot 12 ($kh_0 \approx 0.25$), where the score decreases by 34-59%. We also reiterate that the values listed in Tables 2, 3, and 4 are inherently linked to the hypothetical uncertainty scenarios considered here. Nevertheless, the results obtained from adjusting the SSVD as described in Section 9 are very encouraging.

References

[1] "Piezoelectric characterization of ejecta from shocked tin surfaces," Vogan, W. S., Anderson, W. W., Grover, M., Hammerberg, J. E., King, N. S. P., Lamoreaux, S. K., Macrum, G., Morley, K. B., Rigg, P. A., Stevens, G. D., Turley, W. D., Veeser, L. R., and Buttler, W. T. *J. Appl. Phys.* **98**:113508 (2005).

[2] "Experimental observations on the links between surface perturbation parameters and shock-induced mass ejection," Monfared, S. K., Oró, D. M., Grover, M., Hammerberg, J. E., LaLone, B. M., Pack, C. L., Schauer, M. M., Stevens, G. D., Stone, J. B., Turley, W. D., Buttler, W. T. *J. Appl. Phys.* **116**:063504 (2014).

[3] "(U) An Analytic Study of Piezoelectric Ejecta Mass Measurements," Tregillis, I. L. LA-UR-17-21218.

[4] "(U) Piezoelectric Ejecta Mass Measurements I: General Analytic Study," Tregillis, I. L. LA-CP-18-00246.

[5] "(U) Piezoelectric Ejecta Mass Measurements II: Analytic Study of the RMI+SSVD Ejecta Source Model," Tregillis, I. L. LA-CP-18-00249.

[6] "(U) Piezoelectric Ejecta Mass Measurements III: Cross-Comparison of Theory, Simulation, & Data," Tregillis, I. L. LA-CP-18-00252.

[7] "(U) Piezoelectric Ejecta Mass Measurements IV: Source-Model Predictions for Thresholded Data," Tregillis, I. L. LA-CP-18-00553

[8] "Second shock ejecta measurements with an explosively driven two-shockwave drive," Buttler, W. T., Oró, D. M., Olson, R. T., Cherne, F. J., Hammerberg, J. E., Hixson, R. S., Monfared, S. K., Pack, C. L., Rigg, P. A., Stone, J. B., and Terrones, G. *J. Appl. Phys.* **116**:103519 (2014)

[9] Buttler, W. T. Personal communication, April 12, 2018

[10] "Dynamic comparisons of piezoelectric ejecta diagnostics," Buttler, W. T., Zell-

ner, M. B., Olson, R. T., Rigg, P. A., Hixson, R. S., Hammerberg, J. E., Obst, A. W., Payton, J. R., Iverson, A., and Young, J. *J. Appl. Phys.* **101**:063547 (2007).

[11] "Probing the underlying physics of ejecta production from shocked Sn samples," Zellner, M. B., Vogan McNeil, W., Hammerberg, J. E., Hixson, R. S., Obst, A. W., Olson, R. T., Payton, J. R., Rigg, P. A., Routley, N., Stevens, G. D., Turley, W. D., Veeser, L. and Buttler, W. T. *J. Appl. Phys.* **103**:123502 (2008).

[12] "A Source Model for Ejecta," Hammerberg, James Edward, Cherne, Frank Joseph, Andrews, Malcom John, Ramabrabhu, Praveen, Buttler, William Tillman LA-UR-16-28337